CMS PAS HIN-12-016

CMS Physics Analysis Summary

Contact: cms-pag-conveners-heavyions@cern.ch

2013/04/30

Study of the inclusive production of charged pions, kaons, and protons in p-Pb collisions at $\sqrt{s_{NN}} = 5.02\,\text{TeV}$

The CMS Collaboration

Abstract

Spectra of identified charged hadrons are measured in p-Pb collisions at the LHC at $\sqrt{s_{NN}} = 5.02\,\text{TeV}$. Charged pions, kaons, and protons in the transverse-momentum range $p_{\mathrm{T}} \approx 0.1$–$1.7$ GeV/c and laboratory rapidities $|y| < 1$ are identified via their energy loss in the CMS silicon tracker. The average p_{T} increases rapidly with the mass of the hadron and the charged-particle multiplicity of the event. The fully corrected p_{T} spectra and integrated yields are compared to pp and Pb-Pb data at various collision energies and to several Monte Carlo event generators.

1 Introduction

The study of hadron production has a long history in high-energy particle and nuclear physics, as well as in cosmic-ray physics. The absolute yields and the transverse momentum (p_{T}) spectra of identified hadrons in high-energy hadron-hadron collisions are among the basic physical observables. They can be used to test the predictions for non-perturbative quantum chromodynamics processes like hadronization and soft parton interactions, and their implementation in Monte Carlo (MC) event generators. The dependence of these quantities on the momentum transfer in the collision provides valuable information on multi-parton interactions as well as on other final-state effects. Spectra of identified particles in proton-nucleus collisions also constitute an important reference for high-energy heavy-ion studies, where final-state effects are known to modify the spectral shape and yields of different hadron species [1–4].

The present analysis focuses on the measurement of the p_{T} spectra of charged hadrons, identified mostly via their energy deposits in silicon detectors, in p-Pb collisions at $\sqrt{s} = 5.02\,\mathrm{TeV}$. The analysis procedures are similar to the ones utilized in the measurement of pion, kaon, and proton production in pp collisions at several center-of-mass energies [5].

The central feature of the CMS apparatus is a superconducting solenoid of 6 m internal diameter. Within the field volume are the silicon pixel and strip tracker, the crystal electromagnetic calorimeter, and the brass/scintillator hadron calorimeter. In addition to the barrel and endcap detectors, CMS has extensive forward calorimetry. CMS uses a right-handed coordinate system, with the origin at the nominal interaction point (IP) and the z axis along the counterclockwise beam direction. The pseudorapidity and rapidity of a particle with energy E, momentum p, and momentum along the z axis p_z are defined as $\eta = -\ln\tan(\theta/2)$ where θ is the polar angle with respect to the z axis and $y = \frac{1}{2}\ln[(E+p_z)/(E-p_z)]$, respectively. A more detailed description of CMS can be found in Ref. [6]. The beam pick-up timing for the experiments (BPTX) devices were used to trigger the detector readout. They are located around the beam pipe at a distance of 175 m from the IP on either side, and are designed to provide precise information on the bunch structure and timing of the incoming beam. A steel/quartz-fibre forward calorimeter (HF) covers the $3 < |\eta| < 5$ region. The HF tower segmentation in η and azimuthal angle ϕ is $0.175{\times}0.175$, except for $|\eta|$ above 4.7 where the segmentation is $0.175{\times}0.35$.

Reconstruction of charged particles at CMS is bounded by the acceptance of the tracker ($|\eta| < 2.4$) and by the decreasing tracking efficiency at low momentum ($p > 0.05$, 0.10, 0.20, and $0.40\,\mathrm{GeV}/c$ for e, π, K, and p, respectively), while particle identification capabilities are restricted to $p < 0.15\,\mathrm{GeV}/c$ for electrons, $p < 1.20\,\mathrm{GeV}/c$ for pions, $p < 1.05\,\mathrm{GeV}/c$ for kaons, and $p < 1.70\,\mathrm{GeV}/c$ for protons. Pions are accessible up to a higher momentum than kaons because of their high relative abundance. In view of the (y, p_{T}) regions where pions, kaons and protons can all be identified, the band $-1 < y < 1$ was chosen for this measurement, since it is a good compromise between p_{T} range and y coverage.

2 Data analysis

The data were taken during a 4-hour run with very low multiple-interaction rate (0.15% "pileup") in September 2012, yielding 2.0 million collisions. The beam energies were 4 TeV for protons and 1.58 TeV per nucleon for lead nuclei, resulting in a center-of-mass energy per nucleon pair of $\sqrt{s_{NN}} = 5.02\,\mathrm{TeV}$. Due to the energy difference, the nucleon-nucleon center-of-mass in the p-Pb collisions is not at rest with respect to the laboratory frame, but moves with a velocity $\beta \approx -0.43$ or rapidity -0.46. Since the higher energy proton beam traveled in the clockwise direction, i.e. at $\theta = \pi$, the rapidity of a particle emitted at y_{cm} in the nucleon-nucleon center-

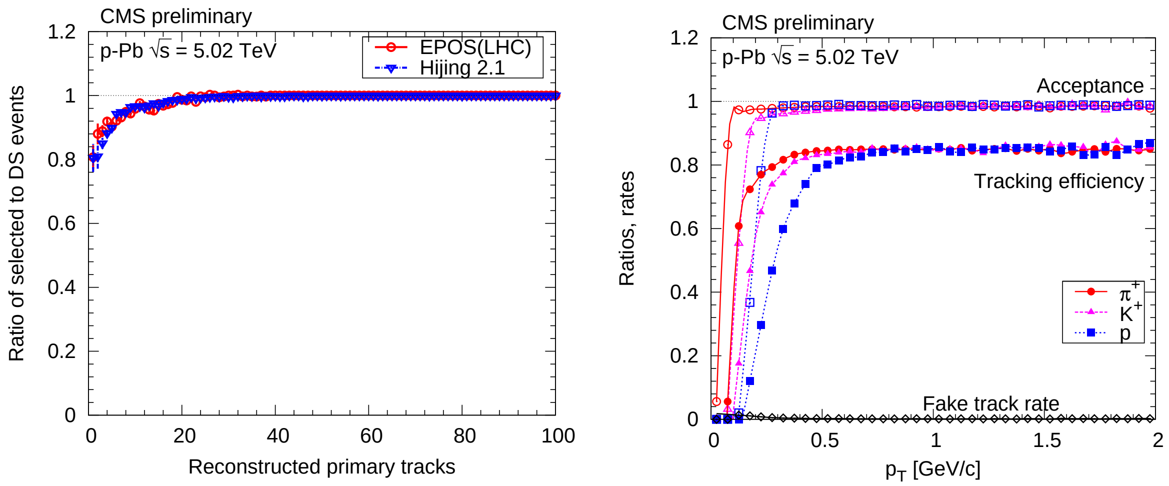

Figure 1: Left: the ratio of selected events to double-sided (DS) events (ratio of the corresponding efficiencies in the inelastic sample), according to EPOS(LHC) [10] and HIJING MC simulations, as a function of the reconstructed primary charged track multiplicity. Right: acceptance, tracking efficiency and fake track rate as a function of p_T for positively charged pions, kaons, and protons based on detector simulations.

of-mass frame is detected in the laboratory frame with a shift, $y_{lab} - y_{cm} = -0.46$, i.e. a particle with $y_{lab} = 0$ moves with rapidity 0.46 in the Pb direction in the center-of-mass system.

The event selection consisted of the following requirements:

- at the trigger level, the coincidence of signals from both BPTX devices, indicating the presence of both proton and lead bunches crossing the interaction point; in addition, at least one track with $p_T > 0.4\,\text{GeV}/c$ in the pixel tracker;
- offline, the presence of at least one tower with energy above 3 GeV in each of the HF calorimeters; at least one reconstructed interaction vertex; beam-halo and beam-induced background events, which usually produce an anomalously large number of pixel hits, are suppressed [7].

The efficiencies for event selection, tracking, and vertexing were evaluated by means of simulated event samples produced with the HIJING [8] MC event generator where the CMS detector response was based on Geant4 [9]. The events were reconstructed in the same way as the collision data. The final results were corrected to a particle level selection, which is very similar to the actual selection described above: at least one particle (proper life time$\tau > 10^{-18}$ s) with $E > 3\,\text{GeV}$ in the range $-5 < \eta < -3$ and one in the range $3 < \eta < 5$; this selection is referred to in the following as “double-sided” (DS) selection. These requirements are expected to suppress single diffractive collisions in the sample. The overall efficiency of the DS selection for the inelastic sample, according to MC event generators studied in this paper (that do not include electromagnetic interactions), is 94-97%.

The ratio of the data selection efficiency to the DS selection efficiency is shown as a function of the reconstructed track multiplicity in Fig. 1-left. The ratio is used to correct the measured events. The results are also corrected for the fraction of DS events without a reconstructed track. This fraction, as given by the simulation, is about 0.1%. Since these events do not contain reconstructed tracks, only the event yield must be corrected.

The extrapolation of particle spectra into the unmeasured (y, p_T) regions is model dependent, particularly at low p_{T}. A good measurement therefore requires reliable track reconstruction down to the lowest possible p_{T}. The present analysis extends to $p_{\mathrm{T}} \approx 0.1\,\mathrm{GeV}/c$ by exploiting special tracking algorithms [11], used in previous studies [5, 7, 12], to provide high reconstruction efficiency and low background rate. The charged pion hypothesis was assumed when fitting particle momenta.

The acceptance of the tracker (when at least two pixel hits are required) is flat in the region $-2 < \eta < 2$ and $p_{\mathrm{T}} > 0.4\,\mathrm{GeV}/c$, and its value is about 96–98% (Fig. 1-right). The loss of acceptance at $p_{\mathrm{T}} < 0.4\,\mathrm{GeV}/c$ is caused by energy loss and multiple scattering of particles, which both depend on the particle mass. Likewise, the reconstruction efficiency is about 75-85%, degrading at low p_{T}, also in a mass-dependent way. The misreconstructed-track rate is very small, reaching 1% only for $p_{\mathrm{T}} < 0.2\,\mathrm{GeV}/c$. The probability of reconstructing multiple tracks from a true single track is about 0.1% – mostly due to particles spiralling in the strong magnetic field. The efficiencies and background rates largely factorize in η and p_{T}, but for the final corrections an (η, p_{T}) matrix is used.

The region where p-Pb collisions occur (beam spot) is well measured by reconstructing vertices from many events. Since the bunches are very narrow, the transverse positions of the interaction vertices are ell constrained; conversely, their z coordinates are spread over a relatively long distance and must be determined on an event-by-event basis. To determine the vertex position, reconstructed tracks are used for determining the vertex position which have $p_{\mathrm{T}} > 0.1\,\mathrm{GeV}/c$ and originate from the vicinity of the beam spot, i.e. their transverse impact parameter satisfies the condition $d_T < 3\sigma_T$; here σ_T is the quadratic sum of the uncertainty in the value of d_T and the RMS of the beam spot distribution in the transverse plane. The agglomerative vertex-reconstruction algorithm [13] was used, with the z coordinates (and their uncertainty) of the tracks at the point of closest approach to the beam axis as input. For single-vertex events, there is no lower limit on the number of tracks associated to the vertex, even one-track vertices are allowed. If multiple vertices are present, only the one with highest multiplicity is kept, since the pileup is negligible.

The distribution of the z coordinates of the reconstructed primary vertices is Gaussian, with standard deviation of 7.1 cm. The simulated data were reweighted so as to have the same vertex z coordinate distribution as the data.

The hadron spectra were corrected for particles of non-primary origin ($\tau > 10^{-12}$ s). The main source of secondary particles is the feed-down from weakly decaying particles, mostly K^0_S, $\Lambda/\overline{\Lambda}$, and $\Sigma^+/\overline{\Sigma}^-$. While the correction is around 1% for pions, it rises up to 15% for protons with $p_{\mathrm{T}} \approx 0.2\,\mathrm{GeV}/c$. As none of the mentioned weakly decaying particles decay into kaons, the correction for kaons is small. Based on studies comparing reconstructed, K^0_S, Λ and $\overline{\Lambda}$ spectra and predictions from the HIJING event generator, both corrections are reweighted by a p_{T} dependent factor. For $p < 0.15\,\mathrm{GeV}/c$, electrons can be clearly identified. The overall $\mathrm{e}^\pm$ contamination of the hadron yields is below 0.2%. Although muons cannot be separated from pions, their fraction is negligible, below 0.05%. Since both contaminations are small, no corrections are applied.

3 Estimation of energy loss rate and yield extraction

In the present paper an analytical parametrization [14] has been used to approximate the energy loss of charged particles in the silicon detectors. The method provides the probability density $p(y|\varepsilon, l)$ of energy deposit y, if the most probable energy loss rate ε at a reference path-length $l_0 = 450\,\mu\mathrm{m}$ and the path-length l are known. It was used in conjunction with a maxi-

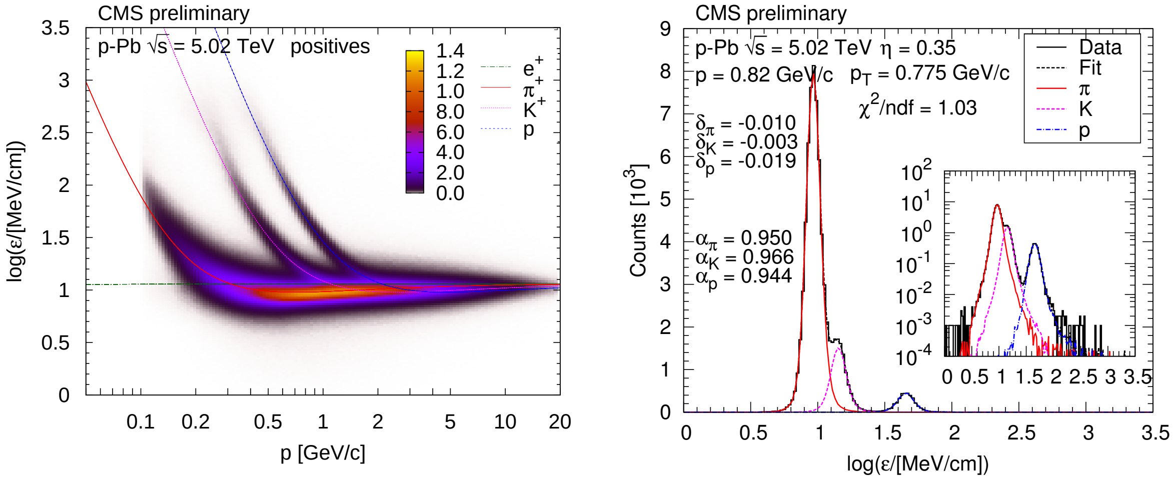

Figure 2: Left: distribution of $\log \varepsilon$ as a function of total momentum p, for positive particles (ε is the most probable energy loss rate at a reference path-length $l_0 = 450\,\mu$m). The z scale is shown in arbitrary units and is linear. The curves show the expected $\log \varepsilon$ for electrons, pions, kaons, and protons [15]. Right: example $\log \varepsilon$ distribution at $\eta = 0.35$ and $p_{\mathrm{T}} = 0.775\,\mathrm{GeV}/c$. Scale factors ($\alpha$) and shifts ($\delta$) are indicated. The inset shows the distribution with logarithmic vertical scale.

mum likelihood estimation.

For pixel clusters, the energy deposits were calculated as the sum of individual pixel deposits. In the case of strips, the energy deposits were corrected for capacitive coupling and cross-talk between neighboring strips. The readout threshold, the coupling parameter, and the standard deviation of the Gaussian noise for strips were determined from data, using tracks with close-to-normal incidence.

For an accurate determination of ε, the response of all readout chips was calibrated with multiplicative gain correction factors. The measured energy deposit spectra were compared to the energy loss parametrization, and hit-level corrections (affine transformation of energy deposits) were introduced. They were applied to individual hits during the determination of the $\log \varepsilon$ fit templates.

The best value of ε for each track was calculated with the corrected energy deposits by minimizing the joint energy deposit negative log-likelihood of all hits on the trajectory (index i), $\chi^2 = -2 \sum_i \log p(y_i | \varepsilon, l_i)$. The $\log \varepsilon$ values in (η, p_{T}) bins were then used in the yield unfolding. Hits with incompatible energy deposits (contributing to the joint χ^2 with a large amount) were excluded. At most one hit was removed; this affected about 1.5% of the tracks. Finally, fit templates, giving the expected $\log \varepsilon$ distributions for all particle species (electrons, pions, kaons, and protons), were built from tracks. All kinematical parameters and hit-related observables were kept, but the energy deposits were re-generated by sampling from the analytical parametrization.

Distributions of $\log \varepsilon$ as a function of total momentum p are plotted in Fig. 2-left for electrons, pions, kaons, and protons, and compared to the predictions of the energy loss method. The remaining deviations were taken into account by means of track-level residual corrections (affine transformation of templates, scale factors and shifts).

Low-momentum particles can be identified unambiguously and can therefore be counted. Conversely, at high momentum, the $\log \varepsilon$ bands overlap (above about $0.5\,\mathrm{GeV}/c$ for pions and kaons, and 1.2 GeV/c for protons); the particle yields therefore need to be determined by means of a series of template fits in $\log\varepsilon$, in bins of η and p_T (Fig. 2-right). For a less biased determination of track-level residual corrections, enhanced samples of each particle type were employed. Some relations and constraints were also exploited, reducing the number of degrees of freedom during the fits: fitting the $\log\varepsilon$ distributions in number of hit (n_{hits}) and track-fit χ^2/ndf slices simultaneously; fixing the distribution n_{hits} of particle species, relative to each other; using the principle of continuity for refinement of track-level residual corrections, in neighboring (η, p_T) bins; using the principle of convergence for track-level residual corrections, as the $\log\varepsilon$ values of two particle species approach each other.

The results of the (iterative) $\log\varepsilon$ fits are the yields for each particle species and charge in bins of (η, p_T) or (y, p_T), both inclusive and divided into classes of reconstructed primary charged track multiplicity. In the end the histogram-fit χ^2/ndf values were usually close to unity. Although pion and kaon yields could not be determined for $p > 1.30$ GeV/c, their sum was measured. This information is an important constraint when fitting the p_T spectra.

The statistical uncertainties for the extracted yields are given by the fits. The observed local variations of parameters in the (η, p_T) plane for track-level corrections cannot be attributed to statistical fluctuations and indicate that the average systematic uncertainties of the scale factors and shifts are about 10^{-2} and $2 \cdot 10^{-3}$, respectively. The systematic uncertainties on the yields in each bin were obtained by refitting the histograms with the parameters changed by these amounts.

4 Corrections and systematic uncertainties

The measured yields in each (η, p_T) bin, $\Delta N_{\text{measured}}$, were first corrected for the misreconstructed-track rate (C_f) and the fraction of secondaries (C_s):

$$\Delta N' = \Delta N_{\text{measured}} \cdot (1 - C_f) \cdot (1 - C_s). \tag{1}$$

The distributions were then unfolded to take into account the finite η and p_T resolutions. The η distribution of the tracks is flat and the η resolution is very good. Conversely, the p_T distribution is steep in the low-momentum region and separate corrections in each η bin were necessary. A straightforward unfolding procedure with linear regularization [16] was used, based on response matrices obtained from MC samples for each particle species.

The corrected yields were obtained by applying corrections for acceptance (C_a), efficiency (C_e), and multiple track reconstruction rate (C_m):

$$\frac{1}{N_{\text{ev}}} \frac{\mathrm{d}^2 N}{\mathrm{d}\eta \mathrm{d}p_T}_{\text{corrected}} = \frac{1}{C_a \cdot C_e \cdot (1 + C_m)} \frac{\Delta N'}{N_{\text{ev}} \Delta\eta \Delta p_T}, \tag{2}$$

where N_{ev} is the corrected number of DS events (Fig. 1). Bins with acceptance smaller than 50%, efficiency smaller than 50%, or multiple-track rate greater than 10% were rejected.

Finally, the differential yields $\mathrm{d}^2N/\mathrm{d}\eta\,\mathrm{d}p_T$ were transformed to invariant yields as a function of the rapidity y by multiplying by the Jacobian E/p, and the (η, p_T) bins were mapped into a (y, p_T) grid. As expected, there is no strong y dependence in the narrow region considered ($|y| < 1$) and therefore the invariant yields $\mathrm{d}^2N/\mathrm{d}\eta\,\mathrm{d}p_T$ as a function of p_T were obtained by averaging over rapidity.

Table 1: Summary of the systematic uncertainties on the p_T spectra. Values in parentheses indicate uncertainties on the $\langle p_\mathrm{T}\rangle$ measurement. Representative, particle-specific uncertainties (π, K, p) are shown at $p_\mathrm{T} = 0.6\,\mathrm{GeV}/c$.

Source	*Uncertainty of the source* [%]	*Propagated yield uncertainty* [%]		
Fully correlated, normalisation				
Correction for event selection	3.0 (1.0)	3.0 (1.0)		
Pileup correction (merged and split vertices)	0.3			
Mostly uncorrelated				
Pixel hit efficiency	0.3	0.3		
Misalignment, different scenarios	0.1			
Mostly uncorrelated, (y, p_T) dependent		π	K	p
Acceptance of the tracker	1–6	1	1	1
Efficiency of the reconstruction	3–6	3	3	3
Multiple-track reconstruction	50% of the corr.	–	–	–
Misreconstructed-track rate	50% of the corr.	0.1	0.1	0.1
Correction for secondary particles	20% of the corr.	0.2	–	2
Fitting $\log \varepsilon$ distributions	1–10	1	2	1

The systematic uncertainties are very similar to those in Ref. [5] and are summarized in Table 1.

5 Results

In previously published measurements of unidentified and identified particle spectra [7, 17], the following form of the Tsallis-Pareto-type distribution [18, 19] was fitted to the data:

$$\frac{\mathrm{d}^2N}{\mathrm{d}y\,\mathrm{d}p_\mathrm{T}} = \frac{\mathrm{d}N}{\mathrm{d}y} \cdot C \cdot p_\mathrm{T}\left[1 + \frac{(m_\mathrm{T} - m)}{nT}\right]^{-n}, \tag{3}$$

where

$$C = \frac{(n-1)(n-2)}{nT[nT + (n-2)m]} \tag{4}$$

and $m_\mathrm{T} = \sqrt{m^2 + p_\mathrm{T}^2}$ (c factors are omitted from the preceding formulae). The free parameters are the integrated yield $\mathrm{d}N/\mathrm{d}y$, the exponent n, and parameter T. The above formula is useful for extrapolating the spectra to $p_\mathrm{T} = 0$, and for extracting $\langle p_\mathrm{T}\rangle$ and $\mathrm{d}N/\mathrm{d}y$. Its validity was cross-checked by fitting MC spectra and verifying that the fitted values of $\langle p_\mathrm{T}\rangle$ and $\mathrm{d}N/\mathrm{d}y$ were consistent with the generated values. According to some models of particle production based on non-extensive thermodynamics [19], the parameter T is connected with the average particle energy, while n characterizes the “non-extensivity” of the process, i.e. the departure of the spectra from a Boltzmann distribution.

As discussed earlier, pions and kaons cannot be unambiguously distinguished at higher momenta. Because of this, the pion-only (kaon-only) $\mathrm{d}^2N/\mathrm{d}y\,\mathrm{d}p_\mathrm{T}$ distribution was fitted for $|y| < 1$ and $p < 1.20\,\mathrm{GeV}/c$ ($p < 1.05\,\mathrm{GeV}/c$); the joint pion and kaon distribution was fitted in the region $|\eta| < 1$ and $1.05 < p < 1.5\,\mathrm{GeV}/c$. Since the ratio p/E for the pions (which are

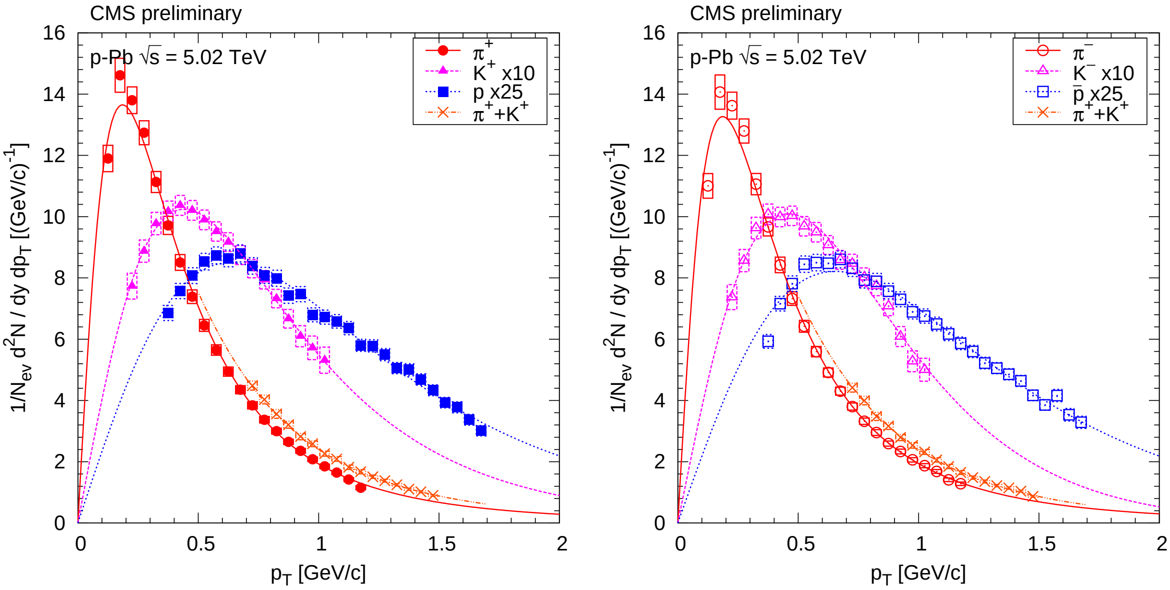

Figure 3: Transverse momentum distributions of identified charged hadrons (pions, kaons, protons) in the range $|y| < 1$, for positive (left) and negative (right) particles. Kaon and proton distributions are scaled as shown in the legends. Fits to Eq. (3) and (5) are superimposed. Error bars indicate the uncorrelated statistical uncertainties, while boxes show the uncorrelated systematic uncertainties. The fully correlated normalisation uncertainty (not shown) is 3.0%.

more abundant than kaons) at these momenta can be approximated by p_T/m_T at $\eta \approx 0$, Eq. (3) becomes:

$$\frac{d^2N}{d\eta dp_T} \approx \frac{dN}{dy} \cdot C \cdot \frac{p_T^2}{m_T} \left(1 + \frac{m_T - m}{nT}\right)^{-n}. \tag{5}$$

The approximate fractions of particles outside the measured p_T range depend on track multiplicity; they are 15–30% for pions, 40–50% for kaons, and 20–35% for protons. The average transverse momentum $\langle p_T \rangle$ and its uncertainty were obtained by numerical integration of Eq. (3) with the fitted parameters, under the assumption that the particle yield distributions follow the Tsallis-Pareto function in the unmeasured p_T region.

The results discussed in the following are for $|y| < 1$. In all cases, error bars indicate the uncorrelated statistical uncertainties, while boxes show the uncorrelated systematic uncertainties. The fully correlated normalisation uncertainty (not shown) is 3.0%. For the p_T spectra, the average transverse momentum, and the ratio of particle yields, the data are compared to AMPT [20], EPOS(LHC) [10], and HIJING MC event generators.

5.1 Inclusive measurements

The transverse momentum distributions of positive and negative hadrons (pions, kaons, protons) are shown in Fig. 3, along with the results of the fits to the Tsallis-Pareto parametrization (Eqs. (3) and (5)). The fits are of good quality with χ^2/ndf values in the range 0.6–2.2. Figure 4 presents the data compared to AMPT, EPOS(LHC), and HIJING. All generators predict steeper p_T distributions than found in data.

Ratios of particle yields as a function of the transverse momentum are plotted in Fig. 5. While

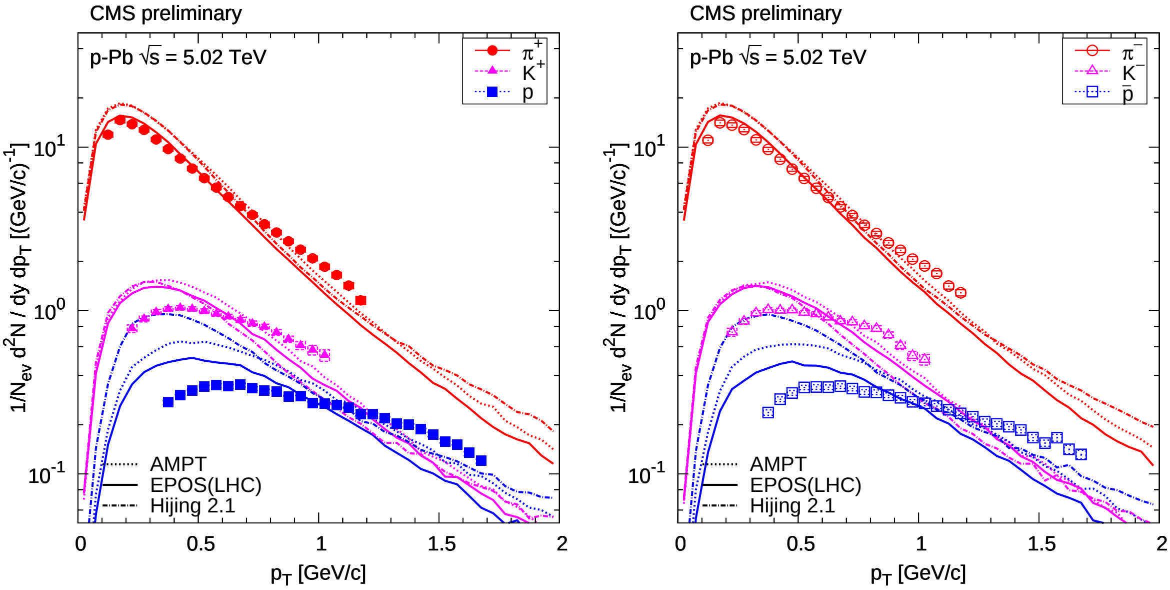

Figure 4: Transverse momentum distributions of identified charged hadrons (pions, kaons, protons) in the range $|y| < 1$, for positive (left) and negative (right) particles. Measured values (same as in Fig. 3) are plotted together with predictions from AMPT, EPOS(LHC), and HIJING. Error bars indicate the uncorrelated statistical uncertainties, while boxes show the uncorrelated systematic uncertainties. The fully correlated normalisation uncertainty (not shown) is 3.0%.

Table 2: Relationship between the number of reconstructed tracks (N_{rec}) and the average number of true tracks ($\langle N_{\text{tracks}} \rangle$) in the region $|\eta| < 2.4$, and also with the condition $p_T > 0.4\,\text{GeV}/c$, in the 19 multiplicity classes considered.

N_{rec}	0-9	10-19	20-29	30-39	40-49	50-59	60-69	70-79	80-89	90-99	100-109	110-119	120-129	130-139	140-149	150-159	160-169	170-179	180-189
$\langle N_{\text{tracks}} \rangle$	8	19	32	45	58	71	84	96	109	122	135	147	160	173	185	198	210	222	235
$\langle (\cdot) \rangle_{p_T > 0.4\,\text{GeV}/c}$	3	8	15	22	29	36	43	50	58	65	73	80	87	95	103	110	117	125	133

the K/π ratios are well described by AMPT and EPOS(LHC), there are substantial deviations for the p/π ratios. The ratios of the yields for oppositely charged particles are close to one, as expected for pair-produced particles at midrapidity.

5.2 Multiplicity-dependent measurements

A study of the dependence on track multiplicity is motivated partly by the intriguing hadron correlations measured in pp and p-Pb collisions at high track multiplicities [21–24], suggesting possible collective effects in "central" pp and p-Pb collisions at the LHC. At the same time it was seen that in pp collisions the characteristics of particle production ($\langle p_T \rangle$, ratios) at LHC energies are strongly correlated with event particle multiplicity rather than with the center-of-mass energy of the collision [5]. In addition, the multiplicity dependence of particle yield ratios is sensitive to various final-state effects (hadronization, color reconnection, collective flow) implemented in MC models used in collider and cosmic-ray physics [25].

The event multiplicity N_{rec} is obtained from the number of reconstructed tracks with $|\eta| < 2.4$,

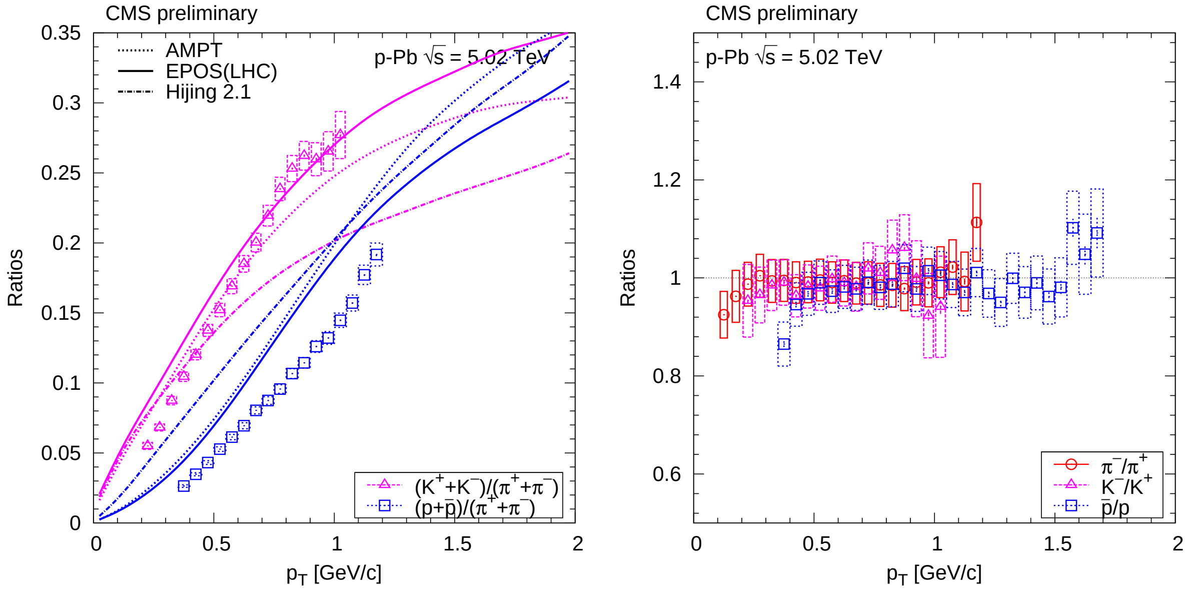

Figure 5: Ratios of particle yields as a function of transverse momentum. Error bars indicate the uncorrelated statistical uncertainties, while boxes show the uncorrelated systematic uncertainties. Curves indicate predictions from AMPT, EPOS(LHC), and HIJING.

where the tracks are reconstructed using the same algorithm as for the identified charged hadrons [11]. (The multiplicity variable $N_{\text{trk}}^{\text{offline}}$, used in Ref. [22], is obtained from a different track reconstruction configuration and a value of $N_{\text{trk}}^{\text{offline}} = 110$ corresponds roughly to $N_{\text{rec}} = 170$.) The event multiplicity was divided into 19 classes, defined in Table 2. To facilitate comparisons with models, the corresponding true charged particle multiplicity in the same acceptance of $|\eta| < 2.4$ (N_{tracks}) is also determined. For each multiplicity class, the correction from N_{rec} to N_{tracks} uses the efficiency from the simulation with HIJING in (η, p_{T}) bins, followed by integration over p_{T} of the corrected data in slices of η (with a linear extrapolation versus p_{T} for $p_{\text{T}} < 0.1\,\text{GeV}/c$), and finished by summing the integrals for each η slice. The average true charged particle multiplicity $\langle N_{\text{tracks}} \rangle$, and also values with the condition $p_{\text{T}} > 0.4\,\text{GeV}$, are shown for each event multiplicity class in Table 2 and is used to identify the multiplicity class in the figures.

The normalized transverse-momentum distributions of identified charged hadrons in selected multiplicity classes for $|y| < 1$ are shown in Fig. 6 for pions, kaons, and protons. The distributions of negatively and positively charged particles have been summed. The distributions are fitted with the Tsallis-Pareto parametrization. In the case of pions, the distributions are remarkably similar, and essentially independent of multiplicity for $N_{\text{tracks}} > 100$. For kaons and protons, the parameter T increases with multiplicity, while for pions both T and the exponent n are independent of multiplicity (not shown).

The ratios of particle yields, obtained by integration of the fitted Tsallis function, are displayed as a function of track multiplicity in Fig. 7. The K/π and p/π ratios are flat, or slightly rising, as a function of N_{tracks}. While none of the models is able to precisely model the track multiplicity dependence, the best and worst match to the overall scale is given by EPOS(LHC) and HIJING, respectively. The ratios of yields of oppositely charged particles are independent of N_{tracks}. The average transverse momentum $\langle p_{\text{T}} \rangle$ is shown as a function of multiplicity in Fig. 8. It is clear that all the event generators presented here underpredict the measured values. For the dependence of T on multiplicity (not shown), the predictions match the pion data well; the

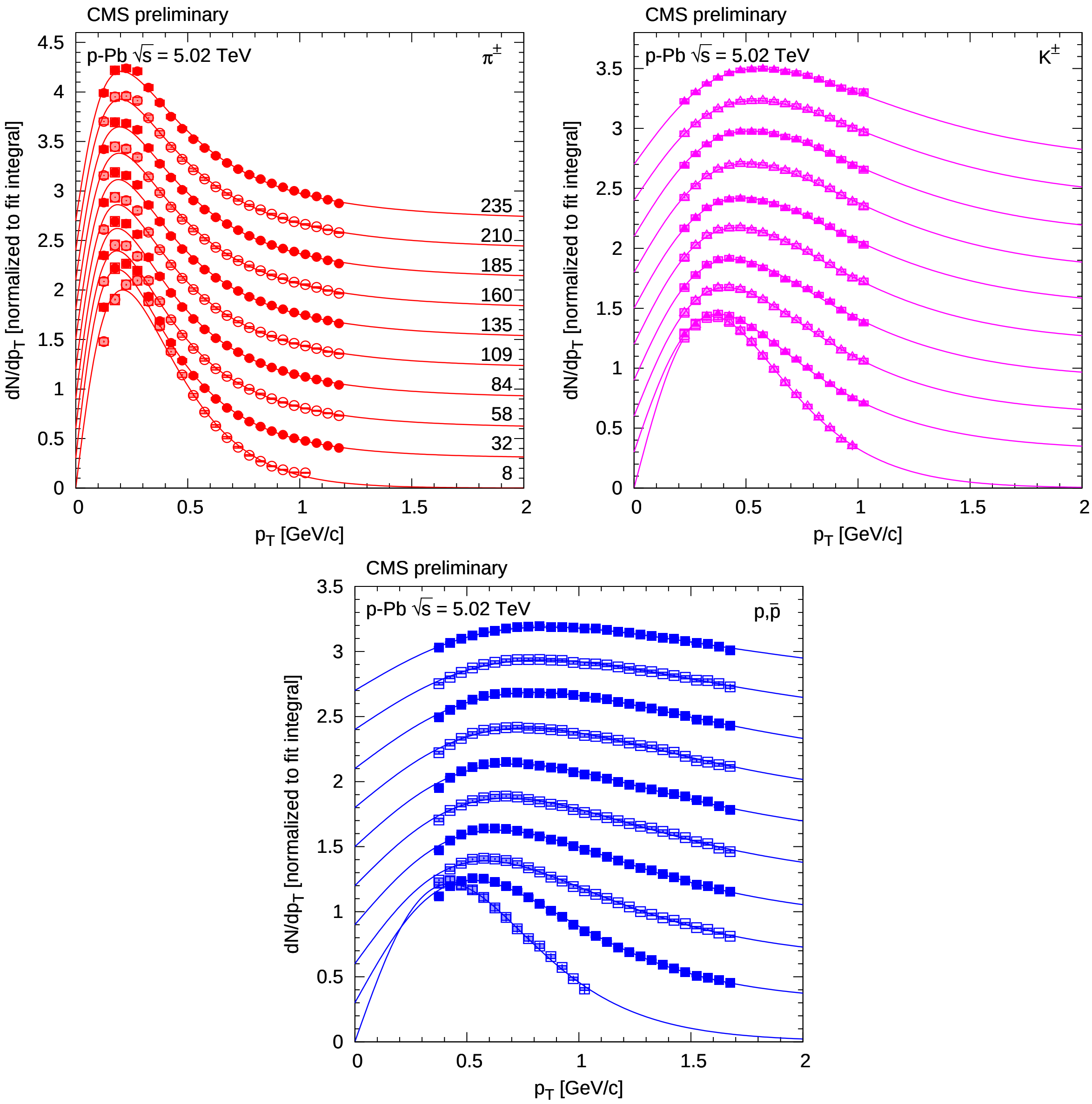

Figure 6: Normalized transverse momentum distributions of charged pions, kaons, and protons in every second multiplicity class ($\langle N_{\text{tracks}} \rangle$ values are indicated for $\pi^{\pm}$), in the range $|y| < 1$, fitted with the Tsallis-Pareto parametrization (solid lines). For better visibility, the result for any given $\langle N_{\text{tracks}} \rangle$ bin is shifted by 0.3 units with respect to the adjacent bins. Error bars indicate the uncorrelated statistical uncertainties, while boxes show the uncorrelated systematic uncertainties.

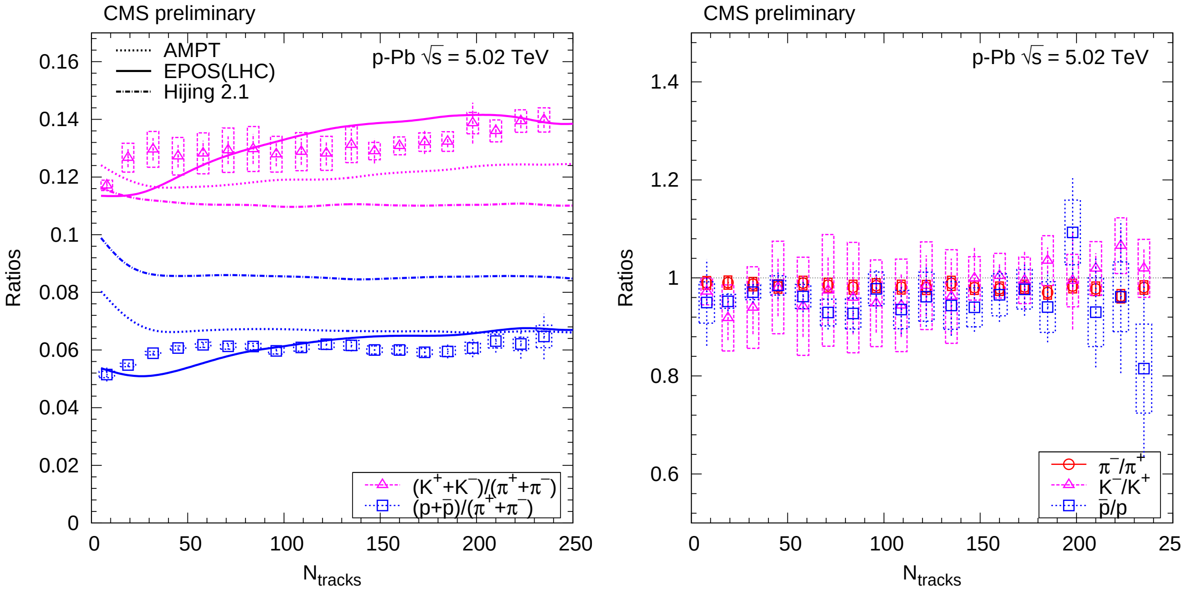

Figure 7: Ratios of particles yields in the range $|y| < 1$ as a function of the true track multiplicity for $|\eta| < 2.4$. Error bars indicate the uncorrelated combined uncertainties, while boxes show the uncorrelated systematic uncertainties. Curves indicate predictions from AMPT, EPOS(LHC), and Hijing.

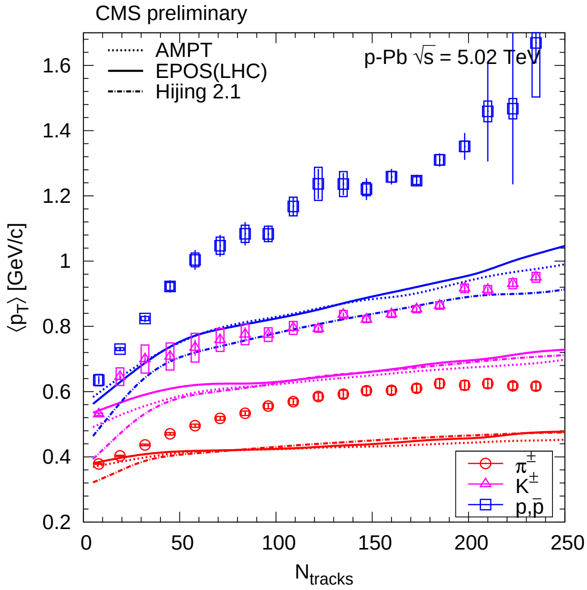

Figure 8: Average transverse momentum of identified charged hadrons (pions, kaons, protons) in the range $|y| < 1$, as a function of the true track multiplicity for $|\eta| < 2.4$. Error bars indicate the uncorrelated combined uncertainties, while boxes show the uncorrelated systematic uncertainties. The fully correlated normalisation uncertainty (not shown) is 1.0%. Curves indicate predictions from AMPT, EPOS(LHC), and Hijing.

kaon and proton values are much higher than in the models.

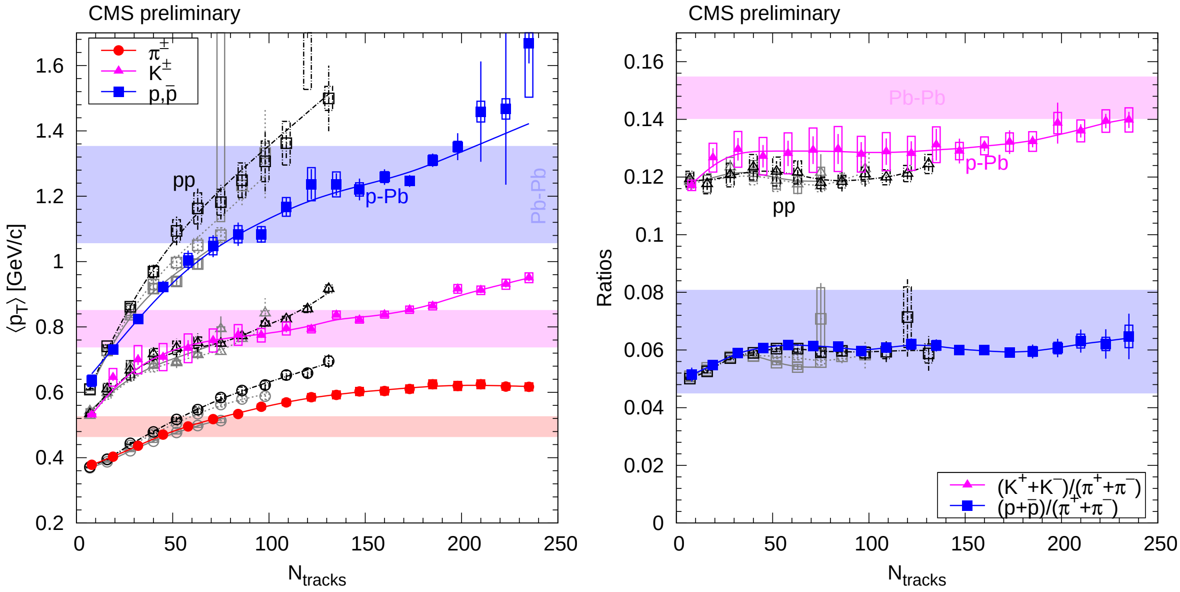

Figure 9: Left: average transverse momentum of identified charged hadrons (pions, kaons, protons) in the range $|y| < 1$, for all particle types, as a function of the true track multiplicity for $|\eta| < 2.4$, for pp collisions at several energies [5], and for p-Pb at $\sqrt{s} = 5.02$ TeV. Right: ratios of particle yields as a function of particle multiplicity for $|\eta| < 2.4$, for pp collisions at several energies [5], and for p-Pb at $\sqrt{s} = 5.02$ TeV. Error bars indicate the uncorrelated combined uncertainties, while boxes show the uncorrelated systematic uncertainties. For $\langle p_T \rangle$ the fully correlated normalisation uncertainty (not shown) is 1.0%. Lines are drawn to guide the eye (gray solid – pp 0.9 TeV, gray dotted – pp 2.76 TeV, black dash-dotted – pp 7 TeV, colored – p-Pb 5.02 TeV). In both plots, the ranges of $\langle p_T \rangle$, K/π and p/π values measured by ALICE in Pb-Pb collisions at $\sqrt{s_{NN}} = 2.76$ TeV [26] are indicated with horizontal bands.

5.3 Comparisons to pp and Pb-Pb data

The comparison with pp data taken at various center-of-mass energies (0.9, 2.76, and 7 TeV) [5] is shown in Fig. 9, where the dependence of $\langle p_T \rangle$ and the particle-yield ratios (K/π and p/π) on the track multiplicity is demonstrated. The plots also display the ranges of these values measured by ALICE in various centrality Pb-Pb collisions at $\sqrt{s_{NN}} = 2.76$ TeV [26]. Although Pb-Pb data are not available at $\sqrt{s_{NN}} = 5.02$ TeV for comparison, the evolution of event characteristics from RHIC ($\sqrt{s_{NN}} = 0.2$ TeV, [2, 4, 27]) to LHC energies [26] indicates that yield ratios should remain similar, while $\langle p_T \rangle$ values will increase by about 5% when going from $\sqrt{s_{NN}} = 2.76$ TeV to 5.02 TeV.

For low track multiplicity ($N_{\text{tracks}} \lesssim 40$), p-Pb collisions behave very similarly to pp collisions, while at higher multiplicities ($N_{\text{tracks}} \gtrsim 50$) the $\langle p_T \rangle$ curve versus multiplicity is flatter. This can be understood, since in the former case mostly peripheral p-Pb collisions are present with a few proton-nucleon collisions. Events with more particles are indicative of collisions in which the projectile proton strikes the thick disk of the lead nucleus. At high multiplicities, p-Pb collisions usually produce particles with smaller $\langle p_T \rangle$ than in pp interactions at similar multiplicity. Interestingly, the p-Pb curves (Fig. 9-left) can be reasonably approximated by taking the pp values and multiplying their N_{tracks} coordinate by a factor of 1.8, for all particles types. In other words, a p-Pb collision with a given N_{tracks} is similar to a pp collision with $0.55 \times N_{\text{tracks}}$ produced charged particles in the $|\eta| < 2.4$ range. Both the highest multiplicity pp and p-Pb interactions yield higher $\langle p_T \rangle$ than in central Pb-Pb collisions. While in the Pb-Pb case even

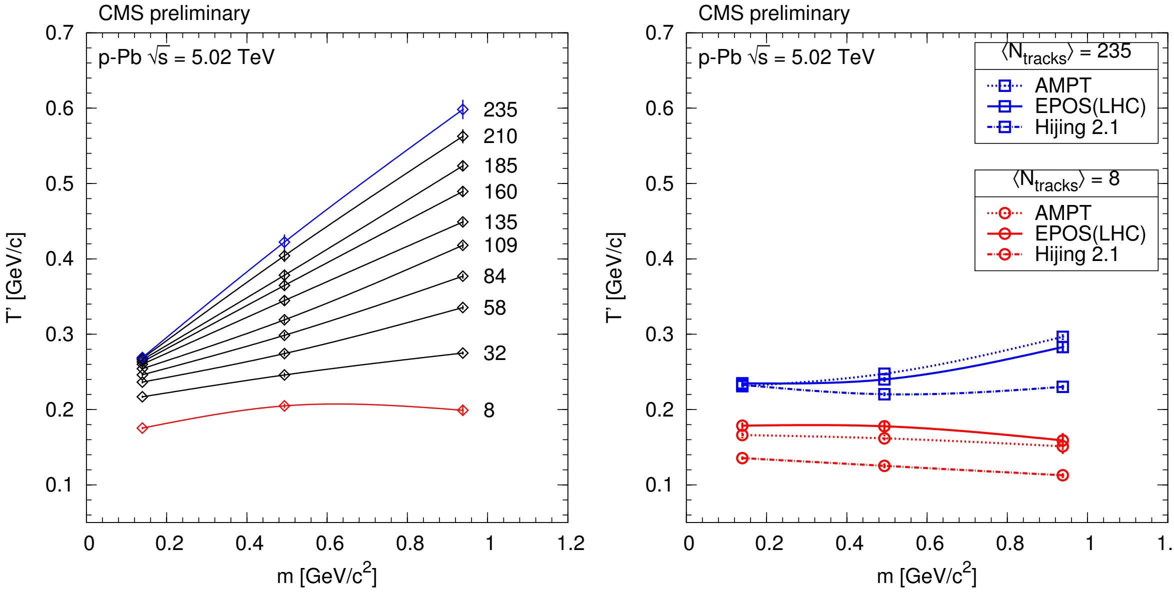

Figure 10: Inverse slope parameters T' from fits of pion, kaon and proton spectra (both charges) with a form proportional to $p_\mathrm{T}\exp(-m_\mathrm{T}/T')$. Results for a selection of multiplicity classes, with N_tracks as indicated, are plotted for p-Pb data (left) and for MC event generators AMPT, EPOS(LHC), and HIJING (right). The curves are drawn to guide the eye.

the most central collisions possibly contain a mix of soft (lower $\langle p_\mathrm{T}\rangle$) and hard (higher $\langle p_\mathrm{T}\rangle$) nucleon-nucleon interactions, for pp or p-Pb collisions the most violent interaction or sequence of interactions are selected.

The transverse momentum spectra could also be successfully fitted with a functional form proportional to $p_\mathrm{T}\exp(-m_\mathrm{T}/T')$, where T' is the inverse slope parameter, motivated by the success of Boltzmann-type distributions in nucleus-nucleus collisions [28]. In case of pions the fitted range was restricted to $m_\mathrm{T} > 0.4\,\mathrm{GeV}/c$. The inverse slope parameter as a function of hadron mass is shown in Fig. 10, for a selection of event classes, both for p-Pb data and for MC event generators (AMPT, EPOS(LHC), and HIJING). While the data display a linear dependence on mass with a slope that increases with particle multiplicity, the models predict a flat behavior versus mass and only small changes with track multiplicity. This is to be compared with pp results [5], where both data and the PYTHIA event generator [29] show features very similar to those in p-Pb data. A similar trend is also observed in nucleus-nucleus collisions [2, 4], which is attributed to the effect of radial flow velocity boost [1].

Rapidity densities $\mathrm{d}N/\mathrm{d}y$ and average transverse momenta $\langle p_\mathrm{T}\rangle$ as a function of center-of-mass energy are shown in Fig. 11 for pp and p-Pb collisions, displaying charge averaged pions, kaons, and protons. To allow comparison at the p-Pb energy, a parabolic (linear) interpolation of the pp collision values at $\sqrt{s} = 0.9$, 2.76, and 7 TeV is shown for $\mathrm{d}N/\mathrm{d}y$ ($\langle p_\mathrm{T}\rangle$). The particle yields in p-Pb collision, obtained with the DS selection, are generally three times greater than in pp interactions at the same energy, while the average transverse momentum increases by about 20%, 10%, and 30% for pions, kaons, and protons, respectively. The factor of three difference in the yields can be compared with the estimated $N_\mathrm{coll}/2 = 3.5 \pm 0.3$ or $N_\mathrm{part}/2 = 4.0 \pm 0.3$, based on preliminary cross-section measurements, that are proven to be good scaling variables in proton-nucleus collisions at lower energies.

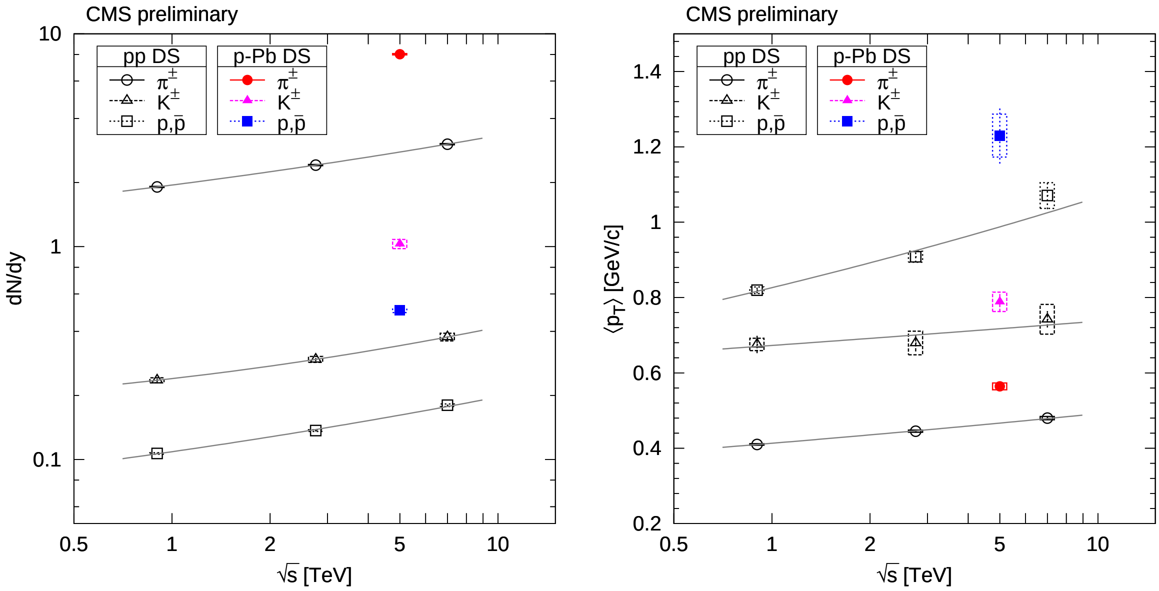

Figure 11: Rapidity densities dN/dy (left) and average transverse momenta $\langle p_T \rangle$ (right) as a function of center-of-mass energy for pp [5] and p-Pb collisions, displaying charged pions, kaons, and protons. Error bars indicate the uncorrelated combined uncertainties, while boxes show the uncorrelated systematic uncertainties. The curves show parabolic (dN/dy) or linear ($\langle p_T \rangle$) interpolation in log-log scale. While in case of pp, data are given for $-1 < y_{cm} < 1$, for p-Pb, measurements in the region $-1 < y_{lab} < 1$ are shown.

6 Conclusions

Measurements of identified charged hadrons produced in p-Pb collisions at $\sqrt{s} = 5.02$ TeV have been presented, based on data collected in events with simultaneous hadronic activity at pseudorapidities $-5 < \eta < -3$ and $3 < \eta < 5$. Charged pions, kaons, and protons were identified from the energy deposited in the silicon tracker and other track information. In the present analysis the data have been studied as a function of the particle multiplicity in the event. The results can be used to further constrain models of hadron production and contribute to the understanding of basic non-perturbative dynamics in hadronic collisions. All studied generators (AMPT, EPOS(LHC), and HIJING) predict steeper p_T distributions and much smaller $\langle p_T \rangle$ than found in data. Also, there are substantial deviations for the p/π ratios.

Combined with similar results from pp collisions [5], the track multiplicity dependence of the average transverse momentum and particle ratios indicates that particle production at LHC energies is strongly correlated with event particle multiplicity in both pp and p-Pb interactions, rather than with the center-of-mass energy of the collision or with the masses of the colliding nuclei. For low track multiplicity, p-Pb collisions appear similar to pp collisions. At high multiplicities, a p-Pb collision with a given N_{tracks} is similar to a pp collision with $0.55 \times N_{tracks}$ produced charged particles in the $|\eta| < 2.4$ range. Both the highest multiplicity pp and p-Pb interactions yield higher $\langle p_T \rangle$ than in central Pb-Pb collisions.

References

[1] E. Schnedermann, J. Sollfrank, and U. W. Heinz, “Thermal phenomenology of hadrons from 200 A/GeV S+S collisions”, *Phys. Rev. C* **48** (1993) 2462–2475,

doi:10.1103/PhysRevC.48.2462, arXiv:nucl-th/9307020.

[2] PHENIX Collaboration, “Identified charged particle spectra and yields in Au+Au collisions at $\sqrt{s_{NN}}$ = 200 GeV”, *Phys. Rev. C* **69** (2004) 034909, doi:10.1103/PhysRevC.69.034909, arXiv:nucl-ex/0307022.

[3] PHOBOS Collaboration, “Identified hadron transverse momentum spectra in Au+Au collisions at $\sqrt{s_{NN}} = 62.4$ GeV”, *Phys. Rev. C* **75** (2007) 024910, doi:10.1103/PhysRevC.75.024910, arXiv:nucl-ex/0610001.

[4] STAR Collaboration, “Systematic Measurements of Identified Particle Spectra in p p, d+Au and Au+Au Collisions from STAR”, *Phys. Rev. C* **79** (2009) 034909, doi:10.1103/PhysRevC.79.034909, arXiv:0808.2041.

[5] CMS Collaboration, “Study of the inclusive production of charged pions, kaons, and protons in pp collisions at $\sqrt{s} = 0.9$, 2.76, and 7 TeV”, *Eur. Phys. J. C* **72** (2012) 2164, doi:10.1140/epjc/s10052-012-2164-1, arXiv:1207.4724.

[6] CMS Collaboration, “The CMS experiment at the CERN LHC”, *JINST* **3** (2008) S08004, doi:10.1088/1748-0221/3/08/S08004.

[7] CMS Collaboration, “Transverse momentum and pseudorapidity distributions of charged hadrons in pp collisions at $\sqrt{s}$ = 0.9 and 2.36 TeV”, *JHEP* **02** (2010) 041, doi:10.1007/JHEP02(2010)041, arXiv:1002.0621.

[8] W.-T. Deng, X.-N. Wang, and R. Xu, “Hadron production in p+p, p+Pb, and Pb+Pb collisions with the HIJING 2.0 model at energies available at the CERN Large Hadron Collider”, *Phys. Rev. C* **83** (2011) 014915, doi:10.1103/PhysRevC.83.014915, arXiv:1008.1841.

[9] S. Agostinelli et al., “Geant4: a simulation toolkit”, *Nucl. Instrum. Meth. A* **506** (2003) 250, doi:10.1016/S0168-9002(03)01368-8.

[10] S. Porteboeuf, T. Pierog, and K. Werner, “Producing Hard Processes Regarding the Complete Event: The EPOS Event Generator”, arXiv:1006.2967.

[11] F. Siklér, “Low p_T Hadronic Physics with CMS”, *Int. J. Mod. Phys. E* **16** (2007) 1819, doi:10.1142/S0218301307007052, arXiv:physics/0702193.

[12] CMS Collaboration, “Transverse-momentum and pseudorapidity distributions of charged hadrons in pp collisions at $\sqrt{s} = 7$ TeV”, *Phys. Rev. Lett.* **105** (2010) 022002, doi:10.1103/PhysRevLett.105.022002, arXiv:1005.3299.

[13] F. Siklér, “Study of clustering methods to improve primary vertex finding for collider detectors”, *Nucl. Instrum. Meth. A* **621** (2010) 526, doi:10.1016/j.nima.2010.04.058, arXiv:0911.2767.

[14] F. Siklér, “A parametrisation of the energy loss distributions of charged particles and its applications for silicon detectors”, *Nucl. Instrum. Meth. A* **691** (2012) 16, doi:10.1016/j.nima.2012.06.064, arXiv:1111.3213.

[15] Particle Data Group Collaboration, “Review of Particle Physics (RPP)”, *Phys. Rev. D* **86** (2012) 010001, doi:10.1103/PhysRevD.86.010001.

[16] W. H. Press et al., "Numerical Recipes: The Art of Scientific Computing". Cambridge University Press, Cambridge, third edition, 2007.

[17] CMS Collaboration, "Strange particle production in pp collisions at $\sqrt{s}$ = 0.9 and 7 TeV", *JHEP* **05** (2011) 064, `doi:10.1007/JHEP05(2011)064`, `arXiv:1102.4282`.

[18] C. Tsallis, "Possible generalization of Boltzmann-Gibbs statistics", *J. Stat. Phys.* **52** (1988) 479, `doi:10.1007/BF01016429`.

[19] T. S. Biró, G. Purcsel, and K. Ürmössy, "Non-extensive approach to quark matter", *Eur. Phys. J. A* **40** (2009) 325, `doi:10.1140/epja/i2009-10806-6`, `arXiv:0812.2104`.

[20] Z. Lin, "Current status and further improvements of a multi-phase transport (AMPT) model", *Indian J. Phys.* **85** (2011) 837–841, `doi:10.1007/s12648-011-0086-7`.

[21] CMS Collaboration, "Observation of long-range near-side angular correlations in proton-proton collisions at the LHC", *JHEP* **09** (2010) 091, `doi:10.1007/JHEP09(2010)091`, `arXiv:1009.4122`.

[22] CMS Collaboration, "Observation of long-range near-side angular correlations in proton-lead collisions at the LHC", *Phys. Lett. B* **718** (2013) 795, `doi:10.1016/j.physletb.2012.11.025`, `arXiv:1210.5482`.

[23] ALICE Collaboration, "Long-range angular correlations on the near and away side in p-Pb collisions at $\sqrt{s_{NN}} = 5.02$ TeV", *Phys. Lett. B* **719** (2013) 29–41, `doi:10.1016/j.physletb.2013.01.012`, `arXiv:1212.2001`.

[24] ATLAS Collaboration, "Observation of Associated Near-side and Away-side Long-range Correlations in $\sqrt{s_{NN}} = 5.02$ TeV Proton-lead Collisions with the ATLAS Detector", `arXiv:1212.5198`. submitted to Phys. Rev. Lett.

[25] D. d'Enterria et al., "Constraints from the first LHC data on hadronic event generators for ultra-high energy cosmic-ray physics", *Astropart. Phys.* **35** (2011) 98, `doi:10.1016/j.astropartphys.2011.05.002`, `arXiv:1101.5596`.

[26] ALICE Collaboration, "Centrality dependence of π, K, p production in Pb-Pb collisions at $\sqrt{s_{NN}}$ = 2.76 TeV", `arXiv:1303.0737`.

[27] BRAHMS Collaboration, "Centrality dependent particle production at $y = 0$ and $y \sim 1$ in Au+Au collisions at $\sqrt{s_{_{NN}}} = 200$ GeV", *Phys. Rev. C* **72** (2005) 014908, `doi:10.1103/PhysRevC.72.014908`, `arXiv:nucl-ex/0503010`.

[28] P. Braun-Munzinger et al., "Hadron production in Au - Au collisions at RHIC", *Phys. Lett. B* **518** (2001) 41–46, `doi:10.1016/S0370-2693(01)01069-3`, `arXiv:hep-ph/0105229`.

[29] T. Sjöstrand, S. Mrenna, and P. Z. Skands, "PYTHIA 6.4 Physics and Manual", *JHEP* **05** (2006) 026, `doi:10.1088/1126-6708/2006/05/026`, `arXiv:hep-ph/0603175`.